A space-time adaptive boundary element method for the wave equation

*A. Aimi, *G. Di Credico, §H. Gimperlein, *C. Guardasoni

*Dept. of Mathematical Physical and Computer Sciences, University of Parma, Italy

*Members of the INdAM-GNCS Research Group, Italy

§Engineering Mathematics, University of Innsbruck, Austria

Abstract

This article initiates the study of space-time adaptive mesh refinements for time-dependent boundary element formulations of wave equations. Based on error indicators of residual type, we formulate an adaptive boundary element procedure for acoustic soft-scattering problems with local tensor-product refinements of the space-time mesh. We discuss the algorithmic challenges and investigate the proposed method in numerical experiments. In particular, we study the performance and improved convergence rates with respect to the energy norm for problems dominated by spatial, temporal or traveling singularities of the solution. The efficiency of the considered rigorous and heuristic a posteriori error indicators is discussed.

1 Introduction

For time-independent problems with singular solutions, adaptive mesh refinements give rise to efficient versions of both finite element and boundary element methods [10, 26], with improved or optimal convergence rates. Correspondingly, for time-dependent problems space- or time-adaptive boundary element methods have attracted much recent interest [17, 18, 23, 28, 40]. However, meshes which are locally refined in both space and time are crucial to resolve space-time singularities such as traveling wave fronts or singularities in nonlinear problems [20]. Partly due to the algorithmic and analytic challenges, such fully space-time adaptive methods have hardly been explored for hyperbolic problems [25].

In this article we initiate the study of fully space-time adaptive mesh refinement procedure for the wave equation, formulated as a boundary integral equation in the time-domain [14, 36]. Based on a posteriori error estimates of residual type [23], the proposed adaptive mesh refinements follows the four steps:

$$\textbf{SOLVE} \longrightarrow \textbf{ESTIMATE} \longrightarrow \textbf{MARK} \longrightarrow \textbf{REFINE}.$$

We here present this fully space-time adaptive method, discuss the involved algorithmic challenges and investigate its properties in numerical experiments.

To describe the main results, we consider the following model problem for the acoustic wave equation

$$\partial_t^2 u - \Delta u = 0 \ , \quad u = 0 \ \text{ for } \ t \leq 0 \ , \tag{1}$$

in the exterior outside an (open or closed) curve $\Gamma \subset \mathbb{R}^2$. The soft-scattering problem imposes inhomogeneous Dirichlet boundary conditions

$$u = f \tag{2}$$

on the obstacle Γ.
Following [7], the problem (1), (2) is equivalent to a time dependent weakly singular integral equation for an unknown density ψ on Γ

$$\mathcal{V}\psi(t,x) = \iint_{\mathbb{R}^+\times\Gamma} G(t-\tau,x,y)\ \psi(\tau,y)\ d\gamma_y\ d\tau = f(t,x)\,, \tag{3}$$

which involves the fundamental solution

$$G(t-\tau,x,y) = \frac{H(t-\tau-|x-y|)}{2\pi\sqrt{(t-\tau)^2-|x-y|^2}} \tag{4}$$

of the wave equation in $\mathbb{R}^2$.

Based on a weak formulation of (3) related to the energy [6], we consider Galerkin discretizations using tensor products of piecewise polynomials in space and time in each space-time element.

Error indicators based on available residual a posteriori error estimates [23] are used to introduce the space-time adaptive algorithm in Subsection 4.1. We address the algorithmic challenges compared to previously studied adaptive methods in space or time separately, which, in particular, exploited the global tensor product structure of the mesh. The proposed adaptive algorithm is studied in numerical experiments. They illustrate the improved convergence rates with respect to the energy norm for problems dominated by spatial, temporal or traveling singularities, with reductions in the required number of degrees of freedom and memory. The experiments indicate the efficiency and reliability of the error estimates in appropriate space-time norms.

The current work contributes to the recent interest in space-time adaptive boundary element methods for the wave equation. For the Dirichlet problem considered in this article, a posteriori error estimates were studied in [23]. However, they were only used for space-adaptive mesh refinements with a uniform time step, while the challenges of fully space-time adaptive refinements were described. Gläfke [25] obtained first computational results towards space-time refinements in $\mathbb{R}^2$. Unpublished work by Abboud uses error estimators of Zienkiewicz-Zhu type [41], as often used in computational engineering, towards space-adaptive mesh refinements for screen problems in $\mathbb{R}^3$. For the Neumann problem, space-adaptive mesh refinements were recently considered in [3].

The literature on adaptive time discretizations to resolve singular temporal behavior is more limited. For the soft scattering problem in $\mathbb{R}$ the adaptive selection of time steps was recently studied in [28, 39, 40], following earlier work [35] in $\mathbb{R}^3$. For time discretizations using convolution quadrature non-uniform time steps have been of much interest. For wave equations, references [29, 30] provided a framework for numerically evaluating the convolution integral with the possibility to accommodate adaptive time stepping. We refer to [13, 31] for first works on adaptive time stepping based on generalized convolution quadrature to solve boundary integral formulations of the time-dependent wave equation.

Beyond adaptive methods, both Galerkin and convolution quadrature methods have attracted much interest for wave equations. Such time domain methods are of particular relevance for problems which cannot be reduced to the frequency domain, including nonlinear problems and problems that involve a broad range of frequencies. We refer to [8, 14, 27, 18] for an overview. Singular solutions have been particularly studied in the case of time-independent geometric singularities, where quasi-optimal convergence rates have been shown for time-independent graded meshes in space or using *hp*-versions on quasi-uniform meshes [4, 22, 19]. Relevant to the current article are works on the efficient assembly and compression of the space-time matrices for both time-stepping and more general space-time discretizations [1, 15, 16, 34, 33, 9, 38], also beyond the classical global tensor product meshes.

Structure of this article: Section 2 introduces the weak formulation of integral equation (3) and its abstract Galerkin discretization. The considered space-time discretizations using local tensor products of piecewise polynomials in space and time are described in Section 3 together with the a posteriori error estimate which is used to define (so-called theoretical) error indicators. Subsequently, algorithmic details are presented in Section 4. Numerical results are collected in

Section 5. They assess the performance and convergence properties of the proposed fully space-time adaptive procedure and the efficiency of the theoretical error indicators, which are further compared with an alternative, heuristic error indicator.

Notation: We write $f \lesssim g$ provided there exists a constant $C > 0$ such that $f \leq Cg$. If the constant C is allowed to depend on a parameter σ, we write $f \lesssim_\sigma g$.

2 Weak formulation of the model problem

We assume that Γ is the boundary of a polygonal Lipschitz domain or an open polygonal Lipschitz curve. The weak formulation of equation (3) involves the bilinear form

$$B(\psi, \phi) = \iint_{\mathbb{R}^+ \times \Gamma} \partial_t \mathcal{V}\psi(t,x)\ \phi(t,x)\ d\gamma_x\, d_\sigma t, \tag{5}$$

where $d_\sigma t = \mathrm{e}^{-2\sigma t} dt$ for fixed $\sigma > 0$.

Remark. The numerical simulations are typically related to a bounded time interval of analysis, where we set $\sigma = 0$ as usual [6, 7].

For the analysis, space-time anisotropic Sobolev spaces provide a convenient framework of function spaces and related norms, going back to [7, 27]. Closely related function spaces were recently also used for the a posteriori analysis of finite element discretizations, see [11, 12]. In particular, the Sobolev space $H^r_\sigma(\mathbb{R}^+, \widetilde{H}^s(\Gamma))$ (essentially) consists of those distributions supported in $\mathbb{R}^+ \times \Gamma$ such that s spatial derivatives and $s+r$ time derivatives belong to $L^2(\mathbb{R}^+ \times \Gamma, d_\sigma t\, d\gamma_x)$. The corresponding Sobolev norm is denoted by $\|\cdot\|_{r,s,\Gamma,*}$. We refer to [4], Appendix A, for precise definitions.

The properties of $B(\cdot,\cdot)$ follow from the properties collected in

Theorem 2.1. *Let $r \in \mathbb{R}$.*

a) *Then the weakly singular operator is continuous,*

$$\mathcal{V} : H^{r+1}_\sigma(\mathbb{R}^+, \widetilde{H}^{-\frac{1}{2}}(\Gamma)) \to H^r_\sigma(\mathbb{R}^+, H^{\frac{1}{2}}(\Gamma))\ . \tag{6}$$

b) *The operator $\partial_t \mathcal{V}$ is weakly coercive:*

$$\iint_{\mathbb{R}^+ \times \Gamma} \partial_t(\mathcal{V}\psi(t,x))\psi(t,x)\ d\gamma_x\ d_\sigma t \gtrsim_\sigma \|\psi\|^2_{0,-\frac{1}{2},\Gamma,*}, \tag{7}$$

and the inverse $\mathcal{V}^{-1}$ is continuous,

$$\mathcal{V}^{-1} : H^{r+1}_\sigma(\mathbb{R}^+, H^{\frac{1}{2}}(\Gamma)) \to H^r_\sigma(\mathbb{R}^+, \widetilde{H}^{-\frac{1}{2}}(\Gamma))\ . \tag{8}$$

This theorem is well-known and documented in [7, 14, 27], as well as [21] when $\partial\Gamma \neq \emptyset$. We conclude that the bilinear form $B(\cdot,\cdot)$ is continuous and weakly coercive:

Proposition 2.2. *For every $\phi, \psi \in H^1_\sigma(\mathbb{R}^+, \widetilde{H}^{-\frac{1}{2}}(\Gamma))$ there holds:*

$$|B(\psi,\phi)| \lesssim \|\psi\|_{1,-\frac{1}{2},\Gamma,*}\|\phi\|_{1,-\frac{1}{2},\Gamma,*} \quad \textit{and} \quad \|\psi\|^2_{0,-\frac{1}{2},\Gamma,*} \lesssim B(\psi,\psi). \tag{9}$$

Proof. The upper bound follows from Theorem 2.1, part a):

$$|B(\psi,\phi)| \leq \|\mathcal{V}\psi\|_{0,\frac{1}{2},\Gamma}\|\partial_t\phi\|_{0,-\frac{1}{2},\Gamma,*} \lesssim \|\psi\|_{1,-\frac{1}{2},\Gamma,*}\|\phi\|_{1,-\frac{1}{2},\Gamma,*}.$$

The lower bound is exactly the assertion in Theorem 2.1, part b). $\square$

Note the loss of a time derivative between the upper and lower estimates and in particular that

$$\|\psi\|^2_{0,-\frac{1}{2},\Gamma,*} \lesssim B(\psi,\psi) \lesssim \|\psi\|^2_{1,-\frac{1}{2},\Gamma,*} \,. \tag{10}$$

Alternative inf-sup stable bilinear forms are discussed in [37].
Then we recall the weak formulation of equation (3):

$$\textit{find} \quad \psi \in H^1_\sigma(\mathbb{R}^+, \widetilde{H}^{-\frac{1}{2}}(\Gamma)) \quad \textit{s.t.} \quad B(\psi,\phi) = \langle \partial_t f, \phi \rangle \quad \forall \phi \in H^1_\sigma(\mathbb{R}^+, \widetilde{H}^{-\frac{1}{2}}(\Gamma)) \,, \tag{11}$$

as well as its Galerkin discretization in a subspace $V_{\Delta t,\Delta x} \subset H^1_\sigma(\mathbb{R}^+, \widetilde{H}^{-\frac{1}{2}}(\Gamma))$:

$$\textit{find } \psi_{\Delta t,\Delta x} \in V_{\Delta t,\Delta x} \textit{ s.t.} \quad B(\psi_{\Delta t,\Delta x}, \phi_{\Delta t,\Delta x}) = \langle \partial_t f, \phi_{\Delta t,\Delta x} \rangle \quad \forall \phi_{\Delta t,\Delta x} \in V_{\Delta t,\Delta x} \,. \tag{12}$$

Corollary 2.3. *Let $f \in H^2_\sigma(\mathbb{R}^+, H^{\frac{1}{2}}(\Gamma))$. The weak formulation (11) and its Galerkin discretization (12) admit unique solutions $\psi \in H^1_\sigma(\mathbb{R}^+, \widetilde{H}^{-\frac{1}{2}}(\Gamma))$ and $\psi_{\Delta t,\Delta x} \in V_{\Delta t,\Delta x}$, respectively.*

3 Discretization

We consider discretizations $\mathcal{T}$ of the space-time cylinder $[0,T] \times \Gamma$ by local tensor products in space and time: $[0,T] \times \Gamma = \bigcup_{S_j \in \mathcal{T}} \overline{S_j}$. Here, the $S_j = I_j \times \Gamma_j$ are pairwise disjoint Cartesian products of a time interval $I_j = [\underline{t}_j, \overline{t}_j)$ and a segment $\Gamma_j \subset \Gamma$. We write $\Delta t_j = \overline{t}_j - \underline{t}_j$ for the size of the local time step and denote the diameter of Γ_j by Δx_j. Further, $\Delta t := \max_j \Delta t_j$, $\Delta x := \max_j \Delta x_j$. On I_j, resp. Γ_j, we consider spaces $V_{\Delta t_j}$ and $V_{\Delta x_j}$ of polynomial functions. The discretization space $V_{\Delta t,\Delta x}$ then consists of functions ψ on $[0,T]\times\Gamma$, such that $\psi|_{S_j} \in V_{\Delta t_j} \otimes V_{\Delta x_j}$, i.e. lies in the tensor product of $V_{\Delta t_j}$ and $V_{\Delta x_j}$, for every S_j.

In our numerical examples, the initial mesh $\mathcal{T}_0$ for the adaptive algorithm is taken to be a global tensor product with $N_t N_x$ space-time elements $S_{(n-1)N_x+i} \equiv I_n \times \Gamma_i$, as represented in Figure 1. For the corresponding discretization space $V^0_{\Delta t,\Delta x}$, we consider the local polynomial degree to be 0, i.e., piecewise constant functions, both in the space and time variables. The basis functions of $V^0_{\Delta t,\Delta x}$ are then given by products of characteristic functions, $\psi_{(n-1)N_x+i}(t,x) := \bar{\psi}_n(t)\bar{\bar{\psi}}_i(x)$, supported on a single element $S_{(n-1)N_x+i}$.

I_{N_t}	$S_{(N_t-1)N_x+1}$	$S_{(N_t-1)N_x+2}$	$S_{(N_t-1)N_x+3}$	$\dots$	$S_{N_tN_x}$
$\vdots$	$\vdots$	$\vdots$	$\vdots$		$\vdots$
I_3	S_{2N_x+1}	S_{2N_x+2}	S_{2N_x+3}	$\dots$	S_{3N_x}
I_2	S_{N_x+1}	S_{N_x+2}	S_{N_x+3}	$\dots$	S_{2N_x}
I_1	S_1	S_2	S_3	$\dots$	S_{N_x}
	Γ_1	Γ_2	Γ_3	$\dots$	Γ_{N_x}

Figure 1: Starting mesh $\mathcal{T}_0$.

Based on an a posteriori error indicator and a marking rule, we will mark selected space-time elements (e.g., in blue in Figure 1). The marked space-time elements are then refined by halving them both in space and in time, as depicted in Figure 2.

<table>
<tr><td>$S_{(N_t-1)N_x+1}$</td><td>$S_{(N_t-1)N_x+2}$</td><td colspan="2">$S_{(N_t-1)N_x+2}$</td><td>$\dots$</td><td>$S_{N_tN_x}$</td></tr>
<tr><td>$\vdots$</td><td>$\vdots$</td><td colspan="2">$\vdots$</td><td></td><td>$\vdots$</td></tr>
<tr><td rowspan="2">S_{2N_x+1}</td><td rowspan="2">S_{2N_x+2}</td><td>$S_{N_tN_x+2}$</td><td>$S_{N_tN_x+3}$</td><td rowspan="2">$\dots$</td><td rowspan="2">S_{3N_x}</td></tr>
<tr><td>S_{2N_x+3}</td><td>$S_{N_tN_x+1}$</td></tr>
<tr><td>S_{N_x+1}</td><td>S_{N_x+2}</td><td colspan="2">S_{N_x+3}</td><td>$\dots$</td><td>S_{2N_x}</td></tr>
<tr><td>S_1</td><td>S_2</td><td colspan="2">S_3</td><td>$\dots$</td><td>S_{N_x}</td></tr>
</table>

Figure 2: Example of mesh refinement.

In this way each marked element S_j is split into 4 smaller space-time elements. We obtain a sequence $\mathcal{T}_k$, $k \geq 1$, of space-time mesh refinements of increasing dimension $N_k = \dim V^k_{\Delta t,\Delta x}$. The basis of $V^k_{\Delta t,\Delta x}$ again is given by the characteristic functions $\psi_j(t,x) = \bar{\psi}_j(t)\bar{\bar{\psi}}_j(x)$, $j = 1,\ldots,N_k$, of $(S_j)_k = (I_j \times \Gamma_j)_k$, i.e. the j-th element of the space-time mesh at refinement level k.

The space-time adaptive algorithm is based on the following a posteriori error estimate (stated in [23]), which involves the restriction of the residual $\mathcal{V}(\psi - \psi_{\Delta t,\Delta x}) =: \mathcal{R}$ to the space-time elements S_j:

Theorem 3.1. *Let $\psi \in H^1_\sigma(\mathbb{R}^+, H^{-\frac{1}{2}}(\Gamma))$ be the solution to (11), and $\psi_{\Delta t,\Delta x}$ the solution to (12). Then*

$$\|\psi - \psi_{\Delta t,\Delta x}\|^2_{0,-\frac{1}{2},\Gamma,*} \lesssim_\sigma \sum_j \max\{\Delta t_j, \Delta x_j\} \left(\|\nabla \mathcal{R}\|^2_{0,0,S_j} + \|\partial_t \mathcal{R}\|^2_{0,0,S_j}\right) =: \sum_j \eta_j^2. \tag{13}$$

The numerical experiments in Section 5 show the efficiency and robustness of this estimate even for the less regular discretization spaces used here.

4 Algorithmic details

4.1 Space-time adaptive algorithm

The a posteriori error estimate from Theorem 3.1 leads to an adaptive mesh refinement procedure, based on the steps:

SOLVE $\longrightarrow$ **ESTIMATE** $\longrightarrow$ **MARK** $\longrightarrow$ **REFINE**.

The precise algorithm we use is given as follows:

Space–Time Adaptive Algorithm:
Input: Datum f, mesh $\mathcal{T}_0$, refinement parameter $\Theta \in (0,1)$, exit tolerance $\epsilon > 0$.

1. $k = 0$.
2. Solve (12) on $\mathcal{T}_k$.
3. Compute the local error indicators η_j^2 in each space-time element $(S_j)_k \in \mathcal{T}_k$ as defined in Theorem 3.1.
4. Stop if $\sum_j \eta_j^2 < \epsilon$.
5. Find $\eta^2_{max} = \max_{j=1,\ldots,N_k} \eta_j^2$, otherwise.
6. Mark all $(S_j)_k \in \mathcal{T}_k$ with $\eta_j^2 > \Theta\, \eta^2_{max}$.
7. Refine each marked $(S_j)_k$ dividing by 2 both in time and space, as shown in Figure 2, obtaining in the end a new mesh $\mathcal{T}_{k+1}$.
8. $k = k + 1$.
9. Go to 2.

Remark. (a) The choice $\Theta = 0$ leads to uniform refinements in space and in time.
(b) A space-adaptive method based on time-integrated error indicators was considered in [23]. As shown in [19, 32], for polyhedral domains and screens time-independent spatially graded meshes with a sufficiently small uniform time step lead to quasi-optimal convergence rates in spite of the singular behavior of the solution at edges and corners.

Finally, since the procedures described in the following subsections hold at each level k of refinement, for the remaining of the Section we will ignore the index k in the notation.

4.2 Algebraic reformulation of the discrete problem

At step 2 of the above written space-time adaptive algorithm, we have to solve (12) on the adaptive mesh of the current level of refinement. Taking into account the notation introduced in Section 3, let us recall that the numerical solution is written as

$$\psi_{\Delta t,\Delta x} := \sum_{j=1}^{N} \alpha_j\, \bar{\psi}_j(t)\bar{\bar{\psi}}_j(x)\,, \quad \text{with} \quad \psi_{\Delta t,\Delta x\,|S_j} = \alpha_j\,. \tag{14}$$

The vector $\boldsymbol{\alpha}$ of coefficients in the linear combination (14) is obtained as solution to the linear system

$$\mathbb{E}\,\boldsymbol{\alpha} = \boldsymbol{\beta}\,, \tag{15}$$

whose matrix entries are defined as

$$\begin{aligned}
\mathbb{E}_{i,j} : &= \int_0^T \int_\Gamma \dot{\bar{\psi}}_i(t)\bar{\bar{\psi}}_i(x) \int_0^t \int_\Gamma \frac{1}{2\pi} \frac{H(t-\tau-|x-y|)}{\sqrt{(t-\tau)^2-|x-y|^2}}\, \bar{\psi}_j(\tau)\bar{\bar{\psi}}_j(y) d\gamma_y\, d\tau\, d\gamma_x\, dt \\
&= \sum_{\mu,\nu=-1}^{0} \int_{\Gamma_i} \bar{\bar{\psi}}_i(x) \int_{\Gamma_j} \bar{\bar{\psi}}_j(y)\ \mathcal{G}(t_{i+\mu}, t_{j+\nu}, |x-y|)\, d\gamma_y\, d\gamma_x\,, \qquad (16)
\end{aligned}$$

where

$$\mathcal{G}(t,\tau,|x-y|) := \frac{1}{2\pi} H(t-\tau-|x-y|)[\log(t-\tau+\sqrt{(t-\tau)^2-|x-y|^2}) - \log(|x-y|)]\,.$$

The elements of the vector $\boldsymbol{\beta}$ on the right hand side of (15) are defined as

$$\beta_i := \int_0^T \int_\Gamma \dot{\bar{\psi}}_i(t)\bar{\bar{\psi}}_i(x) f(t,x)\, d\gamma_x\, dt = \sum_{\mu=-1}^{0} (-1)^{\gamma+1} \int_{\Gamma_j} f(t_{i+\mu}, x)\, d\gamma_x. \tag{17}$$

Observe that the linear system (15) loses the typical block lower triangular Toeplitz structure (see e.g. [6]), which is only available for time independent space meshes and uniform time steps. For the accurate evaluation of the weakly singular integrals in the matrix entries (16), we refer to [6].

To minimize the computational cost, at each refinement step the matrix entries not involved in the refinement are not recomputed. For the sake of clarity, we illustrate the matrix update in case of the refinement depicted in Figure 2. There, the $(2N_x+3)$-th row and column will be replaced by the entries evaluated on a smaller space-time element S_{2N_x+3}, and three new rows and columns, related to the space-time elements denoted by $S_{N_tN_x+1}, S_{N_tN_x+2}, S_{N_tN_x+3}$, are added to the previous matrix.

4.3 Implementation of error indicators

The implementation of the error indicator is based on the evaluation of $\|\nabla\mathcal{R}\|^2_{0,0,S_j}$ and $\|\partial_t\mathcal{R}\|^2_{0,0,S_j}$, where, in this setting,

$$\mathcal{R}(t,x) = f(t,x) - \sum_{i=1}^{N} \alpha_i \int_{\Gamma_i} \int_{t_{i-1}}^{t_i} \frac{1}{2\pi} \frac{H(t-\tau-|x-y|)}{\sqrt{(t-\tau)^2-|x-y|^2}} d\gamma_y d\tau\,. \tag{18}$$

For the time derivative $\partial_t\mathcal{R}(t,x)$, we have

$$\begin{aligned}
\partial_t\mathcal{R}(t,x) &= \partial_t f(t,x) - \sum_{i=1}^{N} \alpha_i \int_{\Gamma_i} \int_{t_{i-1}}^{t_i} -\partial_\tau \left(\frac{1}{2\pi} \frac{H(t-\tau-|x-y|)}{\sqrt{(t-\tau)^2-|x-y|^2}} \right) d\gamma_y d\tau \\
&= \partial_t f(t,x) + \frac{1}{2\pi} \sum_{i=1}^{N} \alpha_i \int_{\Gamma_i} \left(\frac{H(t-t_i-|x-y|)}{\sqrt{(t-t_i)^2-|x-y|^2}} - \frac{H(t-t_{i-1}-|x-y|)}{\sqrt{(t-t_{i-1})^2-|x-y|^2}} \right) d\gamma_y\,.
\end{aligned}$$

In the particular case[1] of $\Gamma = \{(x,0), x \in [0,1]\}$, as considered in the numerical examples, one has $\Gamma_i := [x_{i-1}, x_i]$ and

$$\begin{aligned}
\int_{\Gamma_i} \frac{H(t-\tau-|x-y|)}{\sqrt{(t-\tau)^2-|x-y|^2}}dy &= \int_0^{x_i} \frac{H(t-\tau-|x-y|)}{\sqrt{(t-\tau)^2-|x-y|^2}}dy - \int_0^{x_{i-1}} \frac{H(t-\tau-|x-y|)}{\sqrt{(t-\tau)^2-|x-y|^2}}dy \\
\int_0^{x_i} \frac{H(t-\tau-|x-y|)}{\sqrt{(t-\tau)^2-|x-y|^2}}dy &= \int_{\max(x-t+\tau,0)}^{\min(x,x_i)} \frac{H(\min(x,x_i)-\max(x-t+\tau,0))}{\sqrt{(t-\tau)^2-|x-y|^2}}dy \\
&+ \int_x^{\min(t-\tau+x,x_i)} \frac{H(\min(t-\tau+x,x_i)-x)H(x_i-x)}{\sqrt{(t-\tau)^2-|x-y|^2}}dy \,.
\end{aligned}$$

Integrating analytically and defining

$$\begin{aligned}
&F(t,\tau,x,y) := \\
&H(t-\tau)\Bigg\{\arctan\left(\frac{x-\min(x,y)}{\sqrt{(t-\tau)^2-(x-\min(x,y))^2}}\right)H(\min(x,y)-\max(x-t+\tau,0)) \\
&+\arctan\left(\frac{x-\max(x-t+\tau,0)}{\sqrt{(t-\tau)^2-(x-\max(x-t+\tau,0))^2}}\right)H(\min(x,y)-\max(x-t+\tau,0)) \\
&-\arctan\left(\frac{x-\min(t-\tau+x,y)}{\sqrt{(t-\tau)^2-(x-\min(t-\tau+x,y))^2}}\right)H(\min(t-\tau+x,y)-x)H(y-x)\Bigg\},
\end{aligned}$$

we obtain

$$\begin{aligned}
&\partial_t \mathcal{R}(t,x) = \partial_t f(t,x) \\
&+\frac{1}{2\pi}\sum_{i=1}^N \alpha_i \big(F(t,t_i,x,x_i) - F(t,t_i,x,x_{i-1}) - F(t,t_{i-1},x,x_i) + F(t,t_{i-1},x,x_{i-1})\big) \,.
\end{aligned}$$

The norm

$$\|\partial_t \mathcal{R}\|^2_{0,0,S_j} = \int_{\Gamma_j}\int_{t_{j-1}}^{t_j} \Big(\partial_t \mathcal{R}(t,x)\Big)^2 dxdt$$

is then computed by Gauss quadrature in space and time.
For the gradient $\nabla \mathcal{R}(t,x)$, in the particular case of $\Gamma = \{(x,0), x \in [0,1]\}$ as considered in the numerical examples, we observe that $\nabla \mathcal{R}(t,x) = (\partial_x \mathcal{R}(t,x), 0)$, with

$$\begin{aligned}
\partial_x \mathcal{R}(t,x) &= \partial_x f(t,x) - \sum_{i=1}^N \alpha_i \int_{\Gamma_i}\int_{t_{i-1}}^{t_i} -\partial_y\left(\frac{1}{2\pi}\frac{H(t-\tau-|x-y|)}{\sqrt{(t-\tau)^2-|x-y|^2}}\right)dyd\tau \\
&= \partial_x f(t,x) + \frac{1}{2\pi}\sum_{i=1}^N \alpha_i \int_{t_{i-1}}^{t_i}\left(\frac{H(t-\tau-|x-x_i|)}{\sqrt{(t-\tau)^2-|x-x_i|^2}} - \frac{H(t-\tau-|x-x_{i-1}|)}{\sqrt{(t-\tau)^2-|x-x_{i-1}|^2}}\right)d\tau \,.
\end{aligned}$$

Using that

$$\int_0^{t_i} \frac{H(t-\tau-|x-y|)}{\sqrt{(t-\tau)^2-|x-y|^2}}d\tau = \int_0^{\min(t_i,t-|x-y|)} \frac{H(\min(t_i,t-|x-y|))}{\sqrt{(t-\tau)^2-|x-y|^2}}d\tau$$

and defining

$$\begin{aligned}
S(t,\tau,x,y) &:= \Big(-\log\Big(t-\min(\tau,t-|x-y|)+\sqrt{(t-\min(\tau,t-|x-y|))^2-(x-y)^2}\Big) \\
&+ \log\Big(t+\sqrt{t^2-(x-y)^2}\Big)\Big)H(\min(\tau,t-|x-y|))\,,
\end{aligned}$$

[1]The more general case of a polygonal boundary Γ would require an analysis of the integrals similar to that in [5].

we obtain

$$\partial_x \mathcal{R}(t,x) = \partial_x f(t,x)$$
$$+\frac{1}{2\pi}\sum_{i=1}^{N}\alpha_i\big(S(t,t_i,x,x_i) - S(t,t_{i-1},x,x_i) - S(t,t_i,x,x_{i-1}) + S(t,t_{i-1},x,x_{i-1})\big)\,.$$

The norm

$$\|\partial_x \mathcal{R}\|^2_{0,0,S_j} = \int_{\Gamma_j}\int_{t_{j-1}}^{t_j}\Big(\partial_x \mathcal{R}(t,x)\Big)^2 dx dt$$

is then computed by Gauss quadrature in space and time.

5 Numerical results

In the following numerical experiments we solve (12) on $\Gamma = \{(x,0), x\in[0,1]\}$ for $t\in[0,T] = [0,1]$, using both adaptive and uniform discretizations. The Dirichlet datum f is specified in the respective examples. Unless stated otherwise, the adaptive algorithm is started with a coarse initial mesh $\mathcal{T}_0$ using $\Delta t = \Delta x = 0.25$, i.e., with $N_x = N_t = 4$. The coarsest uniform space-time discretization parameters are given by $\Delta t = \Delta x = 0.1$, i.e., $N_x = N_t = 10$. The adaptive numerical experiments are then based on the space-time adaptive algorithm from Subsection 4.1. In addition to the theoretical local error indicators from Theorem 3.1, i.e., $\eta_j^2 := \max\{\Delta t_j, \Delta x_j\}\ \Big(\|\nabla\mathcal{R}\|^2_{0,0,S_j} + \|\partial_t \mathcal{R}\|^2_{0,0,S_j}\Big)$, we also use heuristic local error indicators defined by

$$\tilde{\eta}_j^2 := \Delta x_j\ \|\nabla\mathcal{R}\|^2_{0,0,S_j} + \|\partial_t\mathcal{R}\|^2_{0,0,S_j}\,. \tag{19}$$

The presented errors are related to the discrete energy defined by

$$E_{\Delta t,\Delta x} := B(\psi_{\Delta t,\Delta x},\psi_{\Delta t,\Delta x}) = \iint_{[0,T]\times\Gamma}\partial_t f(t,x)\ \psi_{\Delta t,\Delta x}(t,x)\ d\gamma_x\, dt\,. \tag{20}$$

The squared errors in energy norm will be plotted with respect to the total number of space-time *DoFs*, together with the corresponding error indicators $\sum_j \eta_j^2$ and $\sum_j \tilde{\eta}_j^2$.

In every example the local error indicators are computed by a Gaussian quadrature rule with 16×16 nodes in each cell of the space-time discretization, to achieve the necessary accuracy.

5.1 Example with smooth benchmark solution

We solve (12) for the Dirichlet datum f which corresponds to the smooth exact solution $\psi(t,x) = xt$, shown on the left of Figure 3. We consider five uniform space-time uniform meshes, obtained from the initial space-time mesh by halving the space and time steps. In this way $\Delta t = \Delta x = 1/N_x = 1/N_t$.

Denoting by $E^{(i)}_{\Delta t,\Delta x}$ the discrete energy obtained for $\Delta x = \Delta t = 1/(10\cdot 2^i)$, we find the empirical rate of convergence for $i = 1,2,3$,

$$\frac{E^{(i+1)}_{\Delta t,\Delta x} - E^{(i)}_{\Delta t,\Delta x}}{E^{(i)}_{\Delta t,\Delta x} - E^{(i-1)}_{\Delta t,\Delta x}} \simeq 4.115$$

and infer a benchmark value $E \approx 0.37135e-01$ for the exact energy.

For the space-time adaptive algorithm the refinement parameter in step 6. is here chosen as $\Theta = 0.2$.

We first consider the decay of the squared L^2 error $\|\psi - \psi_{\Delta t,\Delta x}\|^2_{0,0}$ and of the squared energy error for uniform refinements in terms of $DoFs = N_x N_t$, as depicted in Figure

4. These slopes correspond to an $O(\Delta x)$ decay for the squared L^2 error, an $O(\Delta x^2)$

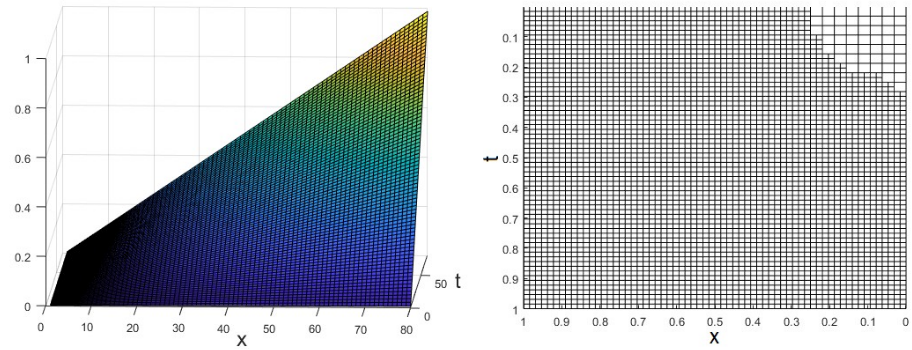

Figure 3: Example 5.1: exact solution (left) and refined mesh (right) using the theoretical error indicator and $\Theta = 0.2$.

decay for the energy error, in agreement with the heuristic indicator, and an $O(\Delta x^3)$ decay for the theoretical error indicator. Hence, we note that the squared error in energy norm, like the heuristic error indicator, behaves as $\Delta x\|\psi - \psi_{\Delta t,\Delta x}\|^2_{0,0} \simeq \|\psi - \psi_{\Delta t,\Delta x}\|^2_{\frac{1}{2},-\frac{1}{2},\Gamma,*}$, while the theoretical error indicator behaves as $\Delta x\Delta t\|\psi - \psi_{\Delta t,\Delta x}\|^2_{0,0}$. Both are greater than or equal to $\|\psi - \psi_{\Delta t,\Delta x}\|^2_{0,-\frac{1}{2},\Gamma,*}$, and the theoretical error indicator estimates a weaker norm than the energy norm, in agreement with the theoretical analysis.

In Figure 5, we show the decay of the energy error in terms of *DoFs* for adaptive space-time refinements, driven respectively by theoretical and heuristic error indicators. The slopes for both energy errors are similar and follow the behavior of the heuristic error indicator, while the theoretical error indicator decays faster, as explained above.

Uniform refinements are quasi-optimal for the smooth solutions like in the current example. Figure 6 accordingly shows the same convergence rate $O(DoFs^{-1})$ of the squared energy errors obtained for the uniform and adaptive refinements. At a fixed number of *DoFs* the error obtained with a uniform mesh is lower. The resulting adaptive refinements are almost uniform in spite of the low value of Θ, as shown in Figure 3 (right) for refinements based on the theoretical error indicator.

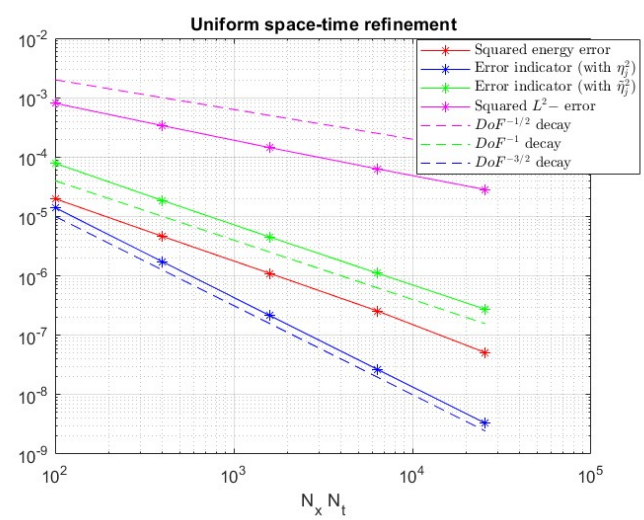

Figure 4: Example 5.1: decay of squared L^2 and energy errors w.r.t. degrees of freedom $DoFs = N_xN_t$.

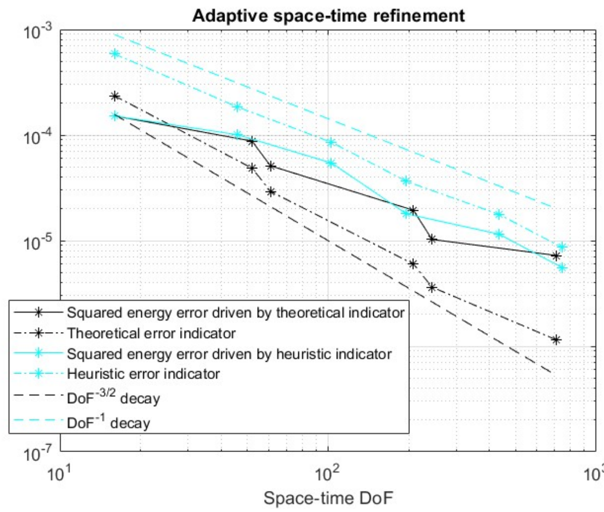

Figure 5: Example 5.1: decay of the energy errors w.r.t. the space-time $DoFs$, driven respectively by theoretical and heuristic error indicators.

5.2 Example with peak-shaped datum

We solve (12) for the Dirichlet datum f shown in Figure 7 on the left, which features a peak and has compact support in a small part of $[0, T] \times \Gamma$:

$$f(t,x) = H(t) \begin{cases} \sin^4(4\pi t) \sin^4\big(3\pi(x-1)\big) H(x-\frac{1}{3}) H(\frac{2}{3}-x) & \text{for} \quad 0 \le t \le \frac{1}{8} \\ \sin^4(4\pi(-t-\frac{2}{8}) \sin^4\big(3\pi(x-1)\big) H(x-\frac{1}{3}) H(\frac{2}{3}-x) & \text{for} \quad \frac{1}{8} \le t \le \frac{2}{8} \\ 0 & \text{for} \quad t \ge \frac{2}{8} \end{cases}$$

The numerical solution is shown in Figure 7 on the right: it features two positive peaks and a negative peak, as well as waves traveling outwards from these peaks in space and time. We expect adaptive mesh refinements along the space-time support of the solution.

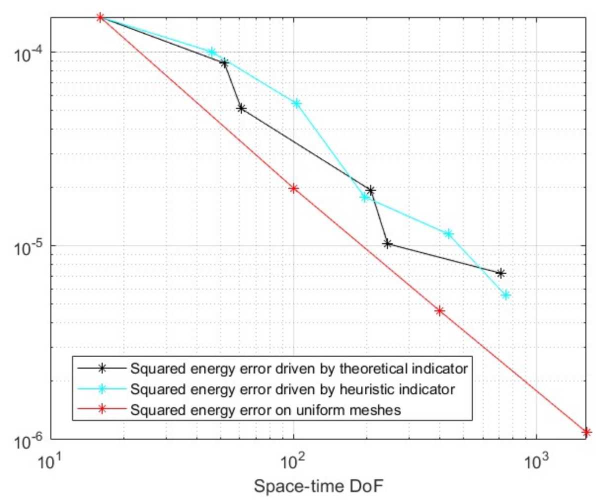

Figure 6: Example 5.1: comparison between the squared energy errors for uniform and adaptive refinements.

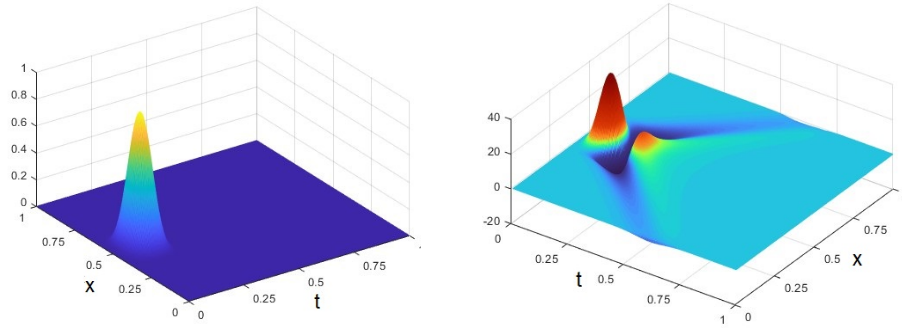

Figure 7: Example 5.2: on the left, peak-shaped Dirichlet datum (left), numerical solution $\psi_{\Delta t,\Delta x}$ obtained with a uniform mesh of $N_x = N_t = 160$ space-time elements (right).

As in the previous example, we consider five uniform space-time uniform meshes, obtained from the initial space-time mesh by halving the space and time steps. In this way $\Delta t = \Delta x = 1/N_x = 1/N_t$. Denoting by $E^{(i)}_{\Delta t,\Delta x}$ the discrete energy obtained for $\Delta x = \Delta t = 1/(10 \cdot 2^i)$, we find the empirical rate of convergence for $i = 1, 2, 3$,

$$\frac{E^{(i+1)}_{\Delta t,\Delta x} - E^{(i)}_{\Delta t,\Delta x}}{E^{(i)}_{\Delta t,\Delta x} - E^{(i-1)}_{\Delta t,\Delta x}} \simeq 3.89$$

and infer a benchmark value $E \approx 3.57403e + 01$ for the exact energy.
For the space-time adaptive algorithm the refinement parameter in step 6. is here chosen as $\Theta = 0.5$.
We first consider the decay of the squared energy error for uniform refinements in terms of $DoFs = N_x N_t$, as depicted in Figure 8. As before, these slopes correspond to an $O(\Delta x^2)$ decay for the energy error, in agreement with the heuristic indicator, and an $O(\Delta x^3)$ decay for the theoretical error indicator.
In Figure 9 we show the decay of the energy error in terms of $DoFs$ for adaptive space-time refinements, driven by the theoretical, respectively heuristic, error indicators.

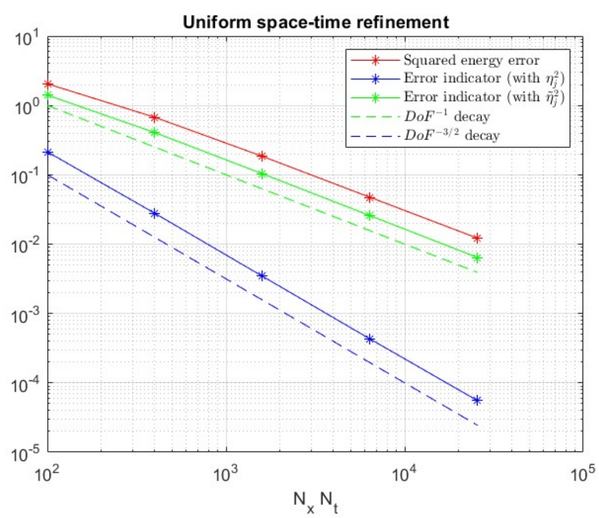

Figure 8: Example 5.2: decay of squared L^2 and energy errors w.r.t. degrees of freedom $DoFs = N_x N_t$.

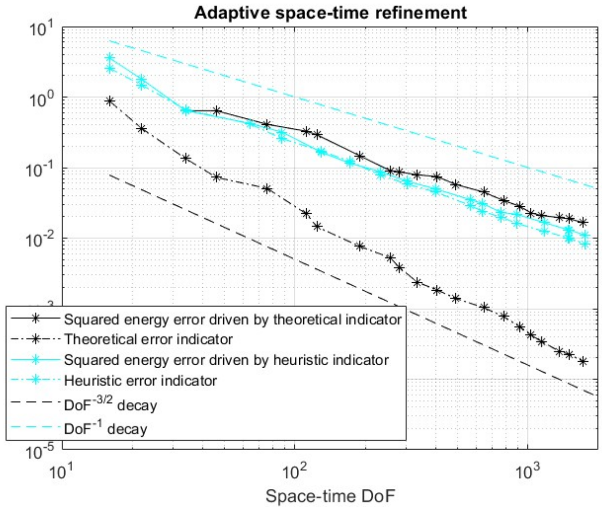

Figure 9: Example 5.2: decay of the energy errors w.r.t. the space-time *DoFs*, driven respectively by theoretical and heuristic error indicators.

It is worth noting that, as in Example 5.1, the convergence of both energy errors is similar and follows the behavior of the heuristic error indicator. Analogous to Example 5.1, the theoretical error indicator decays faster, as analytically expected, estimating a weaker norm.

In Figure 10 we depict an adaptive mesh driven by the theoretical error indicator (left) and the corresponding numerical solution (right) obtained by the adaptive algorithm with exit tolerance $\epsilon = 10^{-5}$.

Figure 11 presents meshes with similar numbers of *DoFs*, obtained using the space-time adaptive algorithm driven respectively by theoretical and heuristic error indicators: both show similar refinements in accordance with the expectations.

Finally, Figure 12 (left) shows a comparison between the squared energy errors obtained by the uniform and adaptive refinements: the slopes for both energy errors are similar, in line with $O(DoFs^{-1})$, as the solution in this example is still smooth. Unlike in Example 5.1, however, because of the features of the solution, at a fixed number of *DoFs* the error obtained from adaptive refinements is significantly lower.

Figure 12 (right) shows the squared energy error decay w.r.t. memory consumption: for the error levels considered, the adaptive refinements also save memory compared to uniform refinements, even though the space-time matrix no longer has a Toeplitz structure. Advantages in memory can only be expected when the adaptive approach leads to a significant reduction of *DoFs*, which overcomes the savings from the Toeplitz structure for uniform meshes, as also in Example 5.4 or problems in $\mathbb{R}^3$.

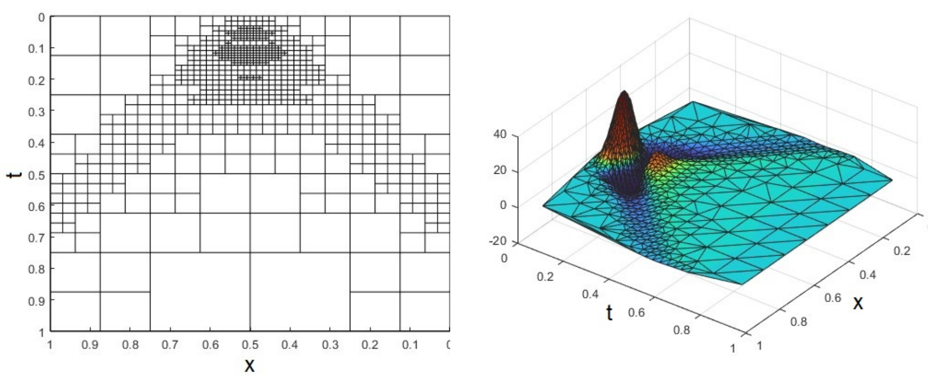

Figure 10: Example 5.2: final mesh driven by theoretical error indicator, obtained by the adaptive algorithm with exit tolerance $\epsilon = 10^{-5}$ (left), corresponding to 15 steps of the Space–Time Adaptive Algorithm, and the numerical solution $\psi_{\Delta t,\Delta x}$ (right).

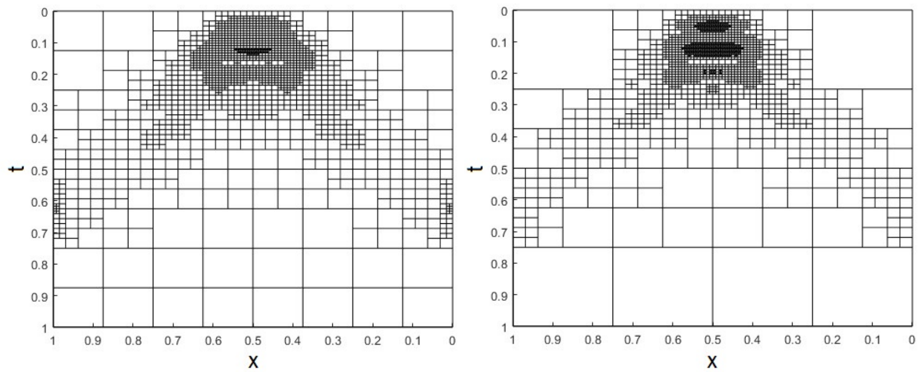

Figure 11: Example 5.2: meshes having similar number of *DoFs*, obtained using adaptive algorithms driven respectively by theoretical (left) and heuristic (right) error indicators with 24 iterations of the Space–Time Adaptive Algorithm.

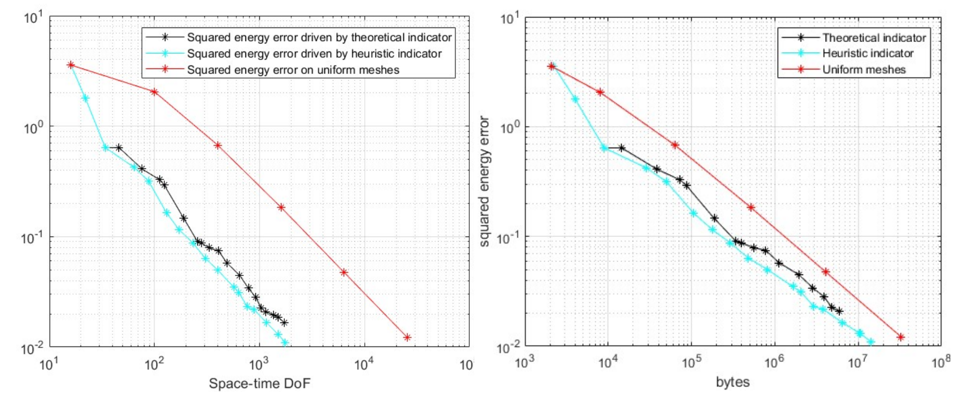

Figure 12: Example 5.2: comparison between the squared energy errors for uniform and adaptive refinements w.r.t. *DoFs* (left) and w.r.t. memory consumption (right).

5.3 Example with solution singular at the endpoints

We solve (12) for the Dirichlet datum f considered in [6], given by

$$f(t,x) = H(t-kx)\begin{cases} \sin^2\big(4\pi(t-kx)\big) & \text{for} \quad 0 \le t-kx \le \frac{1}{8}, \\ 1 & \text{for} \quad t-kx \ge \frac{1}{8}, \end{cases}$$

with $k = \cos(\theta)$ and $\theta \in (0,\pi)$. To be specific, we fix $\theta = \pi/2$.
The numerical solution is shown in Figure 13: near the endpoints of Γ it features the typical geometric singularity, tending to ∞ like the inverse of the square root of the distance to the closest endpoint. The singular behavior is further illustrated by the snapshot of the solution at fixed time $t = 1$ in Figure 14 on the right. The evolution in time in the points $x = 0.4875, 0.9875$ is shown in the same figure on the left, which suggests that adaptive mesh refinements may be expected near $t = 0$, in addition to the endpoints of Γ.
Here we consider six uniform space-time uniform meshes, obtained from the initial space-time mesh by halving the space and time steps. In this way $\Delta t = \Delta x = 1/N_x = 1/N_t$. Denoting by $E^{(i)}_{\Delta t,\Delta x}$ the discrete energy obtained for $\Delta x = \Delta t = 1/(10 \cdot 2^i)$, we find the empirical rate of convergence for $i = 1,2,3$,

$$\frac{E^{(i+1)}_{\Delta t,\Delta x} - E^{(i)}_{\Delta t,\Delta x}}{E^{(i)}_{\Delta t,\Delta x} - E^{(i-1)}_{\Delta t,\Delta x}} \simeq 3.3372$$

and infer a benchmark value $E \approx 2.07339e+01$ for the exact energy.

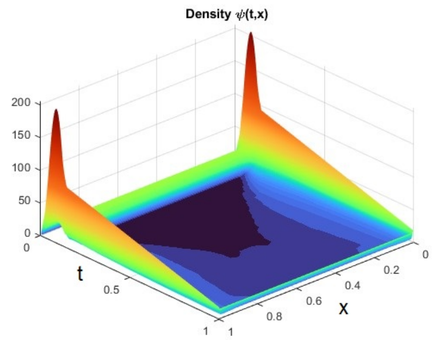

Figure 13: Example 5.3: evolution of numerical solution $\psi_{\Delta t,\Delta x}$ in space and time

For the space-time adaptive algorithm the refinement parameter in step 6. is here chosen as $\Theta = 0.5$.

We first consider the decay of the squared energy error for uniform refinements in terms of $DoFs = N_x N_t$, as depicted in Figure 15. The theoretical error indicator decays as $O(\Delta x)$, as expected for a solution with square-root singularity at the crack tips [19]. The convergence of the squared energy error and the heuristic error indicator is still in a pre-asymptotic regime and, for a growing number of $DoFs$, is expected to approach the slower rate of convergence $O(\Delta x)$. In fact, as the mesh is the same for both error indicators, and since $\eta_j^2 \leq \tilde{\eta}_j^2$ the green line cannot intersect the blue line but can, at most, approach it if $\|\partial_t R\|$ is negligible w.r.t. $\|\nabla R\|$. As the heuristic error indicator is consistent with the squared energy error, asymptotically the red curve is expected to become parallel to the blue one.

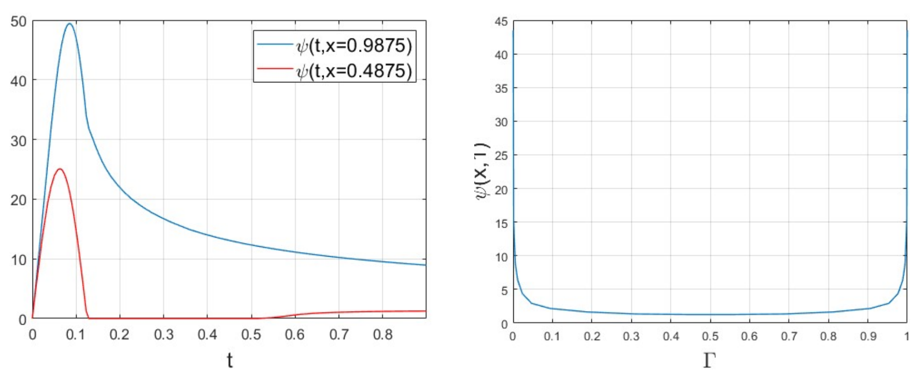

Figure 14: Example 5.3: time profiles of numerical solution $\psi_{\Delta t,\Delta x}$ at $x = 0.4875, 0.9875$ (left), space profile at $t = 1$ (right).

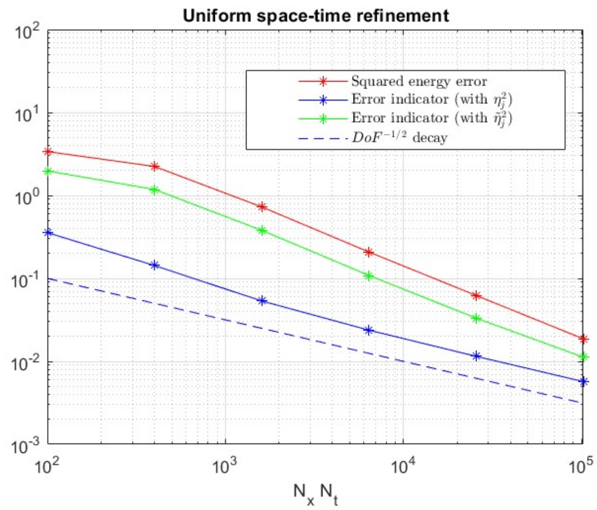

Figure 15: Example 5.3: decay of squared L^2 and energy errors w.r.t. degrees of freedom $DoFs = N_x N_t$

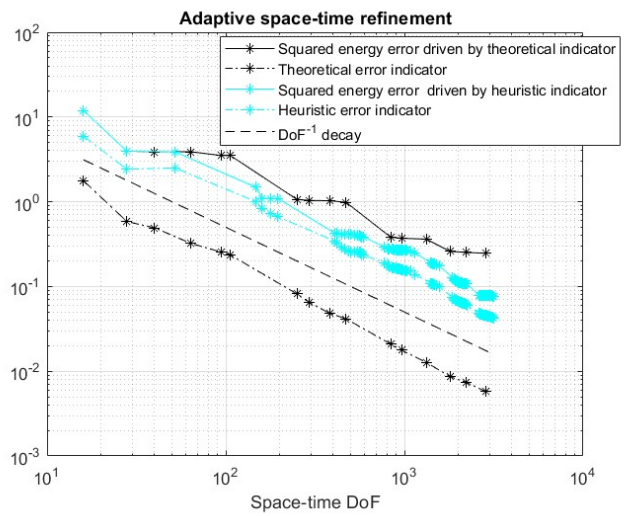

Figure 16: Example 5.3: decay of the energy errors w.r.t. the space-time $DoFs$, driven respectively by theoretical and heuristic error indicators.

In Figure 16 we show the decay of the energy error in terms of $DoFs$ for adaptive space-time refinements, driven by the theoretical, respectively heuristic, error indicators. Unlike in the previous experiments, we find the same convergence rates for both energy errors and their indicators in this problem, indicating the dominant effect of the spatial singularity. Figure 17 shows a comparison between the squared energy errors obtained by the uniform and adaptive refinements: the slopes for the adaptive approaches, in line with $O(DoFs^{-1})$, is about twice the rate $O(DoF^{-1/2})$ of the uniform approach, suggesting the expected convergence [19].
In Figure 18 we finally depict adaptive meshes driven by the theoretical error indicator, for different initial meshes $\mathcal{T}_0$ and different exit tolerances. Both show similar refinements in accordance with the expectations.

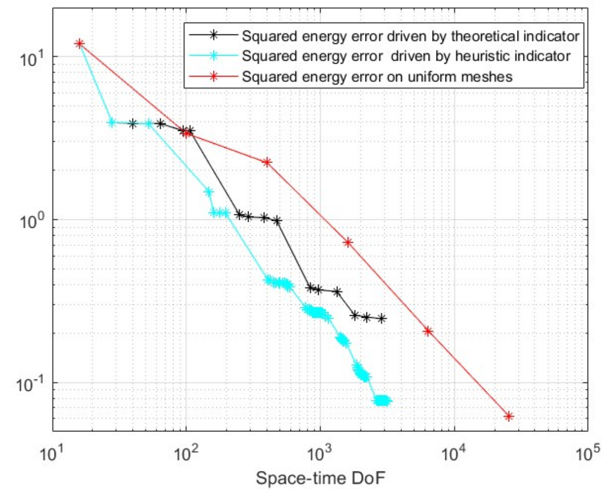

Figure 17: Example 5.3: comparison between the squared energy errors for uniform and adaptive refinements.

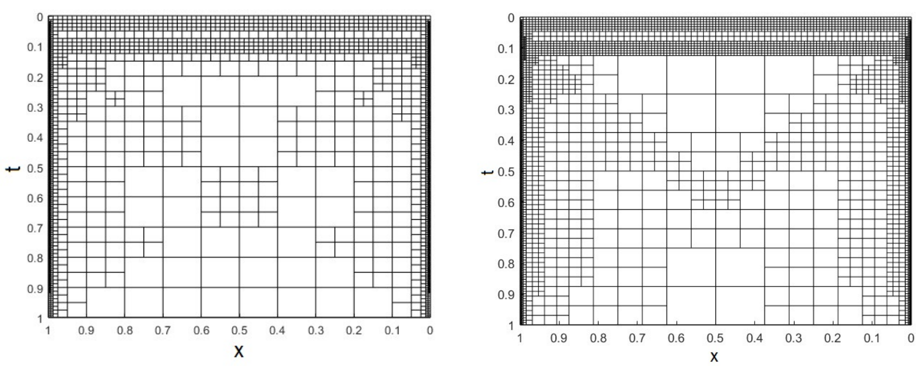

Figure 18: Example 5.3: adaptive meshes driven by theoretical error indicator. On the left: $\mathcal{T}_0$ with $\Delta x = \Delta t = 0.1$ and $\epsilon = 10^{-5}$, on the right: $\mathcal{T}_0$ with $\Delta x = \Delta t = 0.5$ and $\epsilon = 10^{-6}$

5.4 Example with solution singular in space and in time

We solve (12) for the Dirichlet datum f given by $f(t, x) = H(t)t^{2/3}$. As shown in Figure 19, the numerical solution contains the geometric singularity at the endpoints of Γ, as in Example 5.3, as well as a mild time singularity at $t = 0$. Adaptive mesh refinements may therefore be expected near $t = 0$, in addition to the endpoints of Γ.

As in the first two examples, we consider five uniform space-time uniform meshes, obtained from the initial space-time mesh by halving the space and time steps. In this way $\Delta t = \Delta x = 1/N_x = 1/N_t$. Denoting by $E^{(i)}_{\Delta t,\Delta x}$ the discrete energy obtained for $\Delta x = \Delta t = 1/(10 \cdot 2^i)$, we find the empirical rate of convergence for $i = 1, 2, 3$,

$$\frac{E^{(i+1)}_{\Delta t,\Delta x} - E^{(i)}_{\Delta t,\Delta x}}{E^{(i)}_{\Delta t,\Delta x} - E^{(i-1)}_{\Delta t,\Delta x}} \simeq 1.317$$

and infer a benchmark value $E \approx 3.64917$ for the exact energy.

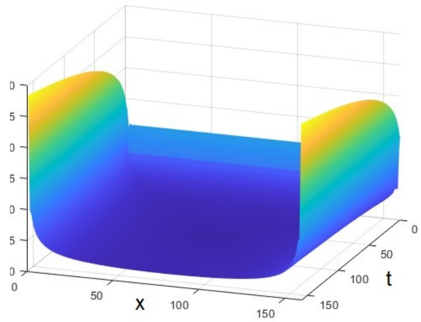

Figure 19: Example 5.4: evolution of the numerical solution $\psi_{\Delta t,\Delta x}$ in space and time.

For the space-time adaptive algorithm the refinement parameter in step 6. is here chosen as $\Theta = 0.5$.

We first consider the decay of the squared energy error for uniform refinements in terms of $DoFs = N_x N_t$, as depicted in Figure 20. The theoretical error indicator converges like $O(\Delta x)$, as expected for a solution with square-root singularity at the crack tips. The squared energy error decays like $O(\Delta x^{1/2})$, in agreement with the heuristic error indicator. In Figure 21 we show the decay of the energy error in terms of $DoFs$ for adaptive space-time refinements driven by the theoretical, respectively heuristic, error indicators. It is worth noting that, as in Examples 5.1 and 5.2, the slopes for both energy errors are similar and follow the behavior of the heuristic indicator, while the theoretical indicator decays faster, as explained in Example 5.1.

Figure 22 presents meshes with similar numbers of $DoFs$, obtained using the space-time adaptive algorithm driven respectively by theoretical and heuristic error indicators: both show similar refinements in accordance with the expectations.

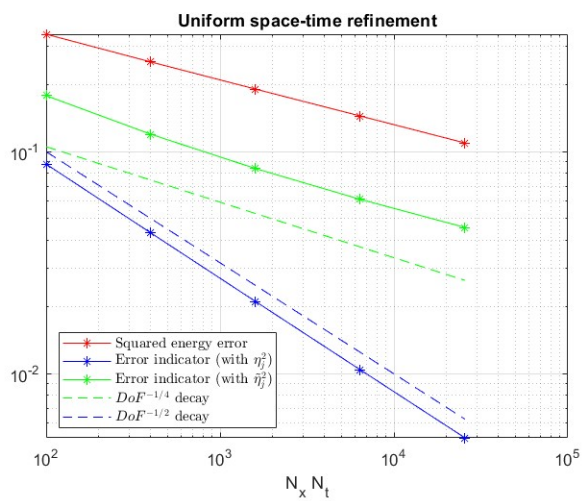

Figure 20: Example 5.4: decay of squared L^2 and energy errors w.r.t. degrees of freedom $DoFs = N_x N_t$.

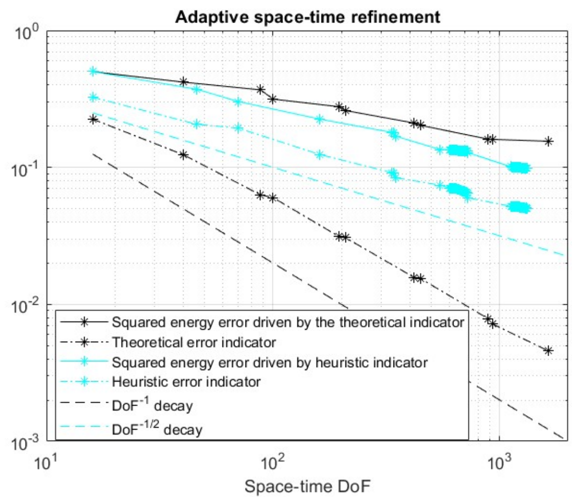

Figure 21: Example 5.4: decay of the energy errors w.r.t. the space-time $DoFs$, driven respectively by theoretical and heuristic error indicators.

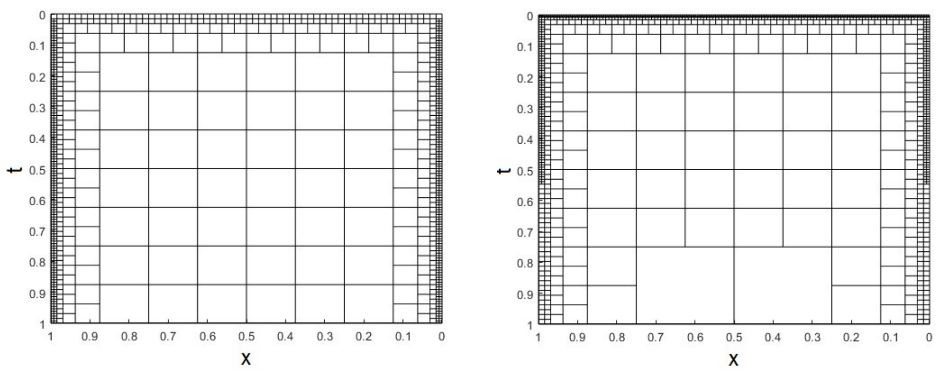

Figure 22: Example 5.4: last mesh of the adaptive algorithm driven by theoretical error indicator (left), last mesh of the adaptive algorithm driven by heuristic error indicator (right)

Finally, Figure 23 (left) shows a comparison between the squared energy errors obtained by the uniform and adaptive refinements: the slopes for the adaptive approaches, in line with $O(DoF^{-1/2})$, are about twice those for the uniform one. This benefit is also reflected in the memory usage, see Figure 23 (right). Despite the overhead for non-product meshes, memory grows more slowly with accuracy in the adaptive cases and memory savings are seen at higher accuracies for both indicators.

6 Conclusions

In this paper we have introduced a space-time adaptive boundary element method for acoustic soft-scattering problems, which are formulated as a weakly singular boundary integral equation. The adaptive mesh refinements are steered by error indicators based on the a posteriori error estimates of residual type in [19] for the $H^0_\sigma(\mathbb{R}^+, H^{-\frac{1}{2}}(\Gamma))$ error, respectively a heuristic modification. Compared to standard implementations for tensor product discretizations of the space-time cylinder $[0,T] \times \Gamma$, we have outlined algorithmic aspects including the efficient assembly of the Galerkin matrix for local tensor products,

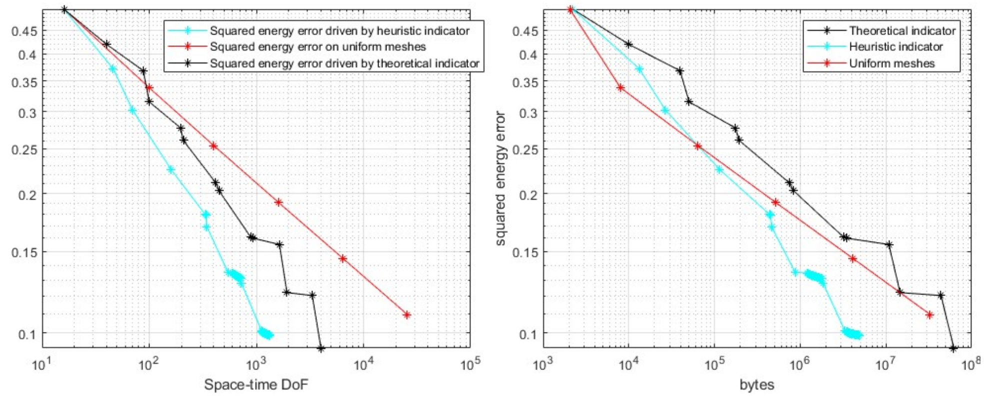

Figure 23: Example 5.4: comparison between the squared energy errors for uniform and adaptive refinements w.r.t. *DoFs* (left) and w.r.t. memory consumption (right).

its update after mesh refinements, as well as the computation of error indicators.
The space-time adaptive algorithm has been studied in numerical experiments for wave scattering problems in $\mathbb{R}^2$ exhibiting a wide range of solutions with singularities in space, in time or in space-time. Numerical results show savings in *DoFs* and in memory, and that the heuristic error indicator converges at the same rate as the energy error, suggesting its efficiency and reliability. Further, they confirm that the theoretical error indicator estimates a weaker norm than the energy norm, as expected from [19], consistent with the expected norm of $H^0_\sigma(\mathbb{R}^+, H^{-\frac{1}{2}}(\Gamma))$, and for uniform refinements the theoretical error indicator leads to the expected convergence rates in all the experiments.
In the case of solutions with power-law singularities the obtained convergence rates on adaptively generated meshes are approximately twice of those obtained on uniform meshes. Like for time-independent problems, higher convergence rates can be achieved on (non-shape regular) graded meshes, but the proposed adaptive algorithm is limited by its shape-regular refinements. Anisotropic space-time refinements may therefore be relevant, but their theoretical basis remains widely open.
This work suggests the promise of an efficient space-time adaptive procedure for wave equations in $\mathbb{R}^3$, where larger savings in *DoFs* and in memory are expected.
Beyond the model problem for the weakly singular integral equation addressed in the current work, future directions of interest include its extension to $\mathbb{R}^3$, to anisotropic mesh refinements and to *hp* methods based on higher-order elements, as well as to nonlinear problems with complex, nonsmooth solutions [2, 24].

Acknowledgments: The authors wish to thank the Centre International de Rencontres Mathématiques (CIRM) in Marseille, France, for support of the research program *Space-time adaptive boundary element methods for wave equations.*

References

[1] A. Aimi, L. Desiderio, and G. Di Credico, *Partially pivoted ACA based acceleration of the energetic BEM for time-domain acoustic and elastic waves exterior problems*, Computers & Mathematics with Applications, 119 (2022), pp. 351–370.

[2] A. Aimi, G. Di Credico, and H. Gimperlein, *Time domain boundary elements for elastodynamic contact*, Computer Methods in Applied Mechanics and Engineering, 415 (2023), p. 116296.

[3] A. Aimi, G. Di Credico, H. Gimperlein, and C. Guardasoni, *Adaptive time-domain boundary element methods for the wave equation with Neumann boundary conditions*, Computers & Mathematics with Applications, 198 (2025), pp. 196–213.

[4] A. Aimi, G. Di Credico, H. Gimperlein, and E. P. Stephan, *Higher-order time domain boundary elements for elastodynamics: graded meshes and hp versions*, Numerische Mathematik, 154 (2023), pp. 35–101.

[5] A. Aimi, M. Diligenti, and C. Guardasoni, *Numerical integration schemes for applications of energetic galerkin BEM to wave propagation problems*, Rivista Matematica dell'Università di Parma, 2 (2011), pp. 147–187.

[6] A. Aimi, M. Diligenti, C. Guardasoni, I. Mazzieri, and S. Panizzi, *An energy approach to space-time Galerkin BEM for wave propagation problems*, Internat. J. Numer. Methods Engrg., 80 (2009), pp. 1196–1240.

[7] A. Bamberger and T. Ha Duong, *Formulation variationnelle espace-temps pour le calcul par potentiel retardé de la diffraction d'une onde acoustique*, Math. Meth. Appl. Sci., 8 (1986), pp. 405–435 and 598–608.

[8] L. Banjai and F.-J. Sayas, *Integral equation methods for evolutionary pde*, Springer Ser. Comput. Math., Springer, Cham, (2022).

[9] S. Bertoluzza, S. Falletta, and L. Scuderi, *Wavelets and convolution quadrature for the efficient solution of a 2d space-time BIE for the wave equation*, Applied Mathematics and Computation, 366 (2020), p. 124726.

[10] A. Bonito, C. Canuto, R. H. Nochetto, and A. Veeser, *Adaptive finite element methods*, Acta Numerica, 33 (2024), pp. 163–485.

[11] T. Chaumont-Frelet, *Asymptotically constant-free and polynomial-degree-robust a posteriori estimates for space discretizations of the wave equation*, SIAM Journal on Scientific Computing, 45 (2023), pp. A1591–A1620.

[12] T. Chaumont-Frelet and A. Ern, *Damped energy-norm a posteriori error estimates using C2-reconstructions for the fully discrete wave equation with the leapfrog scheme*, ESAIM: Mathematical Modelling and Numerical Analysis, 59 (2025), pp. 1937–1972.

[13] L. Cicci, *Step control for the generalized convolution quadrature of the first order*, M.Sc. thesis, University of Rome, 2017.

[14] M. Costabel and F.-J. Sayas, *Encyclopedia of Computational Mechanics, Second Edition*, E. Stein, R. de Borst and J. R. Hughes, 2017, ch. Time-dependent problems with the boundary integral equation method, pp. 1–24.

[15] L. Desiderio and S. Falletta, *Efficient solution of two-dimensional wave propagation problems by CQ-wavelet BEM: algorithm and applications*, SIAM Journal on Scientific Computing, 42 (2020), pp. B894–B920.

[16] V. Domínguez, T. Sánchez-Vizuet, and F.-J. Sayas, *A fully discrete Calderón calculus for the two-dimensional elastic wave equation*, Computers & Mathematics with Applications, 69 (2015), pp. 620–635.

[17] G. Gantner and R. van Venetië, *Adaptive space-time BEM for the heat equation*, Computers & Mathematics with Applications, 107 (2022), pp. 117–131.

[18] H. Gimperlein, M. Maischak, and E. P. Stephan, *Adaptive time domain boundary element methods with engineering applications*, The Journal of Integral Equations and Applications, 29 (2017), pp. 75–105.

[19] H. Gimperlein, F. Meyer, D. Stark, C. Özdemir and E. P. Stephan, *Boundary elements with mesh refinements for the wave equation*, Numerische Mathematik, 139 (2018), pp. 867–912.

[20] H. Gimperlein, F. Meyer, C. Özdemir, and E. P. Stephan, *Time domain boundary elements for dynamic contact problems*, Computer Methods in Applied Mechanics and Engineering, 333 (2018), pp. 147–175.

[21] H. Gimperlein, Z. Nezhi, and E. P. Stephan, *A priori error estimates for a time-dependent boundary element method for the acoustic wave equation in a half-space*, Mathematical Methods in the Applied Sciences, 40 (2017), pp. 448–462.

[22] H. Gimperlein, C. Özdemir, D. Stark, and E. P. Stephan, *hp-version time domain boundary elements for the wave equation on quasi-uniform meshes*, Computer Methods in Applied Mechanics and Engineering, 356 (2019), pp. 145–174.

[23] H. Gimperlein, C. Özdemir, D. Stark, and E. P. Stephan, *A residual a posteriori estimate for the time-domain boundary element method*, Numerische Mathematik, 146 (2020), pp. 239–280.

[24] H. Gimperlein and J. Stocek, *Space–time adaptive finite elements for nonlocal parabolic variational inequalities*, Computer Methods in Applied Mechanics and Engineering, 352 (2019), pp. 137–171.

[25] M. Glaefke, *Adaptive Methods for Time Domain Boundary Integral Equations*, PhD thesis, Brunel University, 2012.

[26] J. Gwinner and E. P. Stephan, *Advanced boundary element methods – treatment of boundary value, transmission and contact problems*, vol. 52 of Springer Series in Computational Mathematics, 2018.

[27] T. Ha Duong, *On retarded potential boundary integral equations and their discretizations*, in Topics in computational wave propagation, Springer, ed., vol. 31 of Lect. Notes Comput. Sci. Eng., Berlin, 2003, p. 301–336.

[28] D. Hoonhout, R. Löscher, O. Steinbach, and C. Urzúa-Torres, *Stable least-squares space-time boundary element methods for the wave equation*. arxiv:2312.12547, 2023.

[29] M. Lopez-Fernandez and S. Sauter, *Generalized convolution quadrature with variable time stepping*, IMA Journal of Numerical Analysis, 33 (2013), pp. 1156–1175.

[30] M. Lopez-Fernandez and S. Sauter, *Generalized convolution quadrature with variable time stepping. part ii: Algorithm and numerical results*, Applied Numerical Mathematics, 94 (2015), pp. 88–105.

[31] A. B. Menon and M. Schanz, *Adaptive time stepping for generalized convolution quadrature*, PAMM, 23 (2023), p. e202300084.

[32] F. Müller and C. Schwab, *Finite elements with mesh refinement for wave equations in polygons*, J. Comp. Appl. Math., 283 (2015), pp. 163–181.

[33] D. Pölz and M. Schanz, *Space-time discretized retarded potential boundary integral operators: quadrature for collocation methods*, SIAM Journal on Scientific Computing, 41 (2019), pp. A3860–A3886.

[34] D. Pölz and M. Schanz, *On the space-time discretization of variational retarded potential boundary integral equations*, Computers & Mathematics with Applications, 99 (2021), pp. 195–210.

[35] S. Sauter and A. Veit, *Adaptive time discretization for retarded potentials*, Numer. Math., 132 (2016), pp. 569–595.

[36] F.-J. Sayas, *Retarded potentials and time domain boundary integral equations: A road map*, vol. 50 of Springer Series in Computational Mathematics, 2016.

[37] O. Steinbach and C. Urzúa-Torres, *A new approach to space-time boundary integral equations for the wave equation*, SIAM J. on Mathematical Analysis, 54 (2022), pp. 1370–1392.

[38] A. Veit, M. Merta, J. Zapletal, and D. Lukas, *Efficient solution of time-domain boundary integral equations arising in sound-hard scattering*, Internat. J. Numer. Meth. Eng., 107 (2016), pp. 430–449.

[39] M. Zank, *Inf-sup stable space-time methods for time-dependent partial differential equations*, Verlag der Technischen Universität Graz, 2020.

[40] M. Zank and O. Steinbach, *Adaptive space-time boundary element methods for the wave equation*, PAMM, 16 (2016), pp. 777–778.

[41] O. C. Zienkiewicz and J. Z. Zhu, *The superconvergent patch recovery and a posteriori error estimates. part 2: Error estimates and adaptivity*, International Journal for Numerical Methods in Engineering, 33 (1992), pp. 1365–1382.